

# Design study and spectroscopic performance of SOI pixel detector with a pinned depleted diode structure for X-ray astronomy

Masataka Yukumoto<sup>a,\*</sup>, Koji Mori<sup>a</sup>, Ayaki Takeda<sup>a</sup>, Yusuke Nishioka<sup>a</sup>, Syuto Yonemura<sup>a</sup>, Daisuke Izumi<sup>a</sup>, Uzuki Iwakiri<sup>a</sup>, Takeshi G. Tsuru<sup>b</sup>, Ikuo Kurachi<sup>c</sup>, Kouichi Hagino<sup>d</sup>, Yasuo Arai<sup>e</sup>, Takayoshi Kohmura<sup>f</sup>, Takaaki Tanaka<sup>g</sup>, Miraku Kimura<sup>a</sup>, Yuta Fuchita<sup>a</sup>, Taiga Yoshida<sup>a</sup>, Tomonori Ikeda<sup>b</sup>

<sup>a</sup> Department of Applied Physics, Faculty of Engineering, University of Miyazaki, 1-1 Gakuen-Kibanadai-Nishi, Miyazaki, 889-2192, Japan

<sup>b</sup> Department of Physics, Faculty of Science, Kyoto University, Kitashirakawa Oiwake-cho, Sakyo-ku, Kyoto 606-8502, Japan

<sup>c</sup> D&S Inc., 774-3-213 Higashiasakawacho, Hachioji, Tokyo 193-0834, Japan

<sup>d</sup> Department of Physics, University of Tokyo, 7-3-1 Hongo, Bunkyo, Tokyo 113-0033, Japan

<sup>e</sup> Accelerator Laboratory, High Energy Accelerator Research Organization (KEK), 1-1 Oho, Tsukuba 305-0801, Japan

<sup>f</sup> Department of Physics and Astronomy, Faculty of Science and Technology, Tokyo University of Science, 2641 Yamazaki, Noda, Chiba 278-8510, Japan

<sup>g</sup> Department of Physics, Konan University, 8-9-1 Okamoto, Higashinada, Kobe, Hyogo 658-8501, Japan

---

## Abstract

We have been developing silicon-on-insulator (SOI) pixel detectors with a pinned depleted diode (PDD) structure, named “XRPIX”, for X-ray astronomy. The PDD structure is formed in a thick p-type substrate, to which high negative voltage is applied to make it fully depleted. A pinned p-well is introduced at the backside of the insulator layer to reduce a dark current generation at the Si-SiO<sub>2</sub> interface and to fix the back-gate voltage of the SOI transistors. An n-well is further introduced between the p-well and the substrate to make a potential barrier between them and suppress a leakage current. An optimization study on the n-well dopant concentration is necessary because a higher dopant concentration could result in a higher potential barrier but also in a larger sense-node capacitance leading to a lower spectroscopic performance, and vice versa. Based on a device simulation, we fabricated five candidate chips having different n-well dopant concentrations. We successfully found out the best n-well design, which suppressed a large leakage current and showed satisfactory X-ray spectroscopic performance. Too low and too high n-well dopant concentration chips showed a large leakage current and degraded X-ray spectroscopic performance, respectively. We also found that the dependency of X-ray spectroscopic performance on the n-well dopant concentration can be largely explained by the difference in sense-node capacitance.

**Keywords:** X-ray detectors, X-ray SOIPIX, Monolithic active pixel sensors, Silicon on insulator technology

---

## 1. Introduction

CCD detectors have been the main instruments of past and current operating X-ray observatories for the last three decades [1, 2, 3, 4, 5, 6] and will be still actively used for new X-ray observatories [7, 8]. CCD detectors are a nearly technically complete instrument and show spectroscopic performance close to the Fano limit of silicon detectors. CCD detectors are expected to continue to advance in the direction of large format and fast readout maintaining the high spectroscopic performance. On the other hand, mostly driven by commercial

imaging application, CMOS detectors have achieved major advances with the modern silicon processing technology. Compared to CCD detectors, CMOS detectors are characterized by their lower power consumption and ability to be realized as a system large-scale integration by incorporating advanced signal processing circuitry. These characteristics are not only highly advantageous for simplifying instrument systems but also provide with new potentials beyond CCD detectors.

We have been developing a new silicon pixel CMOS detector, called XRPIX, for X-ray astronomy [9]. XRPIX utilizes silicon-on-insulator (SOI) technology, which combines a thick high-resistivity silicon sensor layer and a high-speed low-resistivity silicon circuit layer via a buried oxide (BOX) layer in a single

---

\*Corresponding author

Email address: yukumoto@astro.miyazaki-u.ac.jp  
(Masataka Yukumoto)

monolithic detector [10]. The most distinctive feature of XRPIX compared to other silicon pixel detectors is that a self-trigger function is incorporated by taking advantage of CMOS technology [11]. This function enables XRPIX to achieve a time resolution of 10  $\mu$ sec or higher. With this high time resolution and surrounding veto counters, the anti-coincidence technique can be utilized to significantly reduce non-X-ray background events due to cosmic rays, which hampers the detection of faint X-ray emission in the case of CCD detectors [12].

The history of the XRPIX development is almost a history of improvement of its spectroscopic performance [9]. We experienced several important progresses so far and the latest one was provided by incorporating a Pinned Depleted Diode (PDD) structure in the sensor layer [13, 14]. Radiation hardness is also significantly improved as well [15, 16]. The PDD structure of XRPIX is formed in a high-negative-bias applied p-type substrate. There exists a pinned p-well under the BOX layer and a depleted n-well between the p-well and the substrate. The n-well acts as a potential barrier to prevent a leakage current from the p-well to the substrate. The details of the PDD structure are given in the next section. An optimization study of the n-well dopant concentration is necessary because higher dopant concentration could result in a higher potential barrier but also in a larger sense-node capacitance leading to a lower spectroscopic performance, and vice versa. In addition, the prototype XRPIX chips with the PDD structure used a rarely available high-resistivity substrate ( $>25$  k $\Omega$  cm) [13, 14]. The resistivity of substrates affects the back bias voltage ( $V_{bb}$ ) required for full depletion, and  $V_{bb}$  affects the height of the potential barrier the n-well makes. Therefore, the resistivity of substrates is also related to the optimization. In this paper, we report the experimental results of the optimization study fabricating five chips with different n-well dopant concentrations using moderate-resistivity substrates ( $\leq 10$  k $\Omega$  cm) that are consistently available in future. Section 2 describes the details of the PDD structure. Section 3 gives the simulation study of n-well dopant concentration and the specification of the five candidate chips. Section 4 presents the basic characteristics and X-ray spectroscopic performance of the chips. Then, Section 5 discusses the relation between the sense-node capacitance and the X-ray spectroscopic performance. Finally, Section 6 concludes this study.

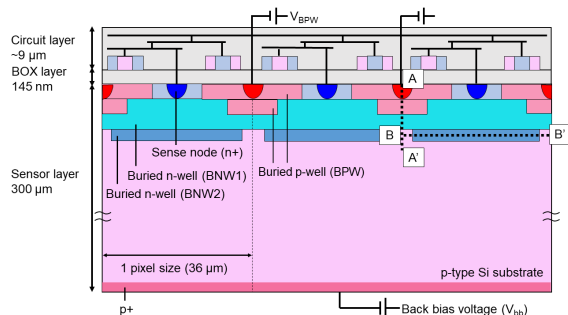


Figure 1: Cross-sectional view of XRPIX8. Two dotted lines, A–A' and B–B', indicate lines, along which potential profiles are drawn in Figures 2(a) and 3, respectively.

## 2. Device structure and description

Figure 1 shows a cross-sectional view of XRPIX8, one of the XRPIX series with the PDD structure. It consists of three layers: a 9  $\mu$ m thick circuit layer including five level interconnects and about 40 nm SOI transistors consisting of low-resistivity silicon, a 300  $\mu$ m thick sensor layer consisting of high-resistivity silicon, and a 145 nm thick BOX layer between the two layers. A high negative voltage is applied at the backside of the sensor layer to fully deplete the substrate. A buried p-well (BPW) is introduced at the backside of the BOX layer. The neutralized BPW is effective for reducing the dark current generation at the Si-SiO<sub>2</sub> interface between the BOX layer and the sensor layer. It shares the same concept as that of a pinned photodiode commonly used in CCD and CMOS image sensors. The BPW, pinned to a fixed bias of  $V_{BPW}$ , also acts as a shielding layer between the sense node and the circuit layer, preventing extra noise from transistors. A buried n-well (BNW1) introduced just under the BPW is depleted. The most important role of the BNW1 is to suppress a large current from the BPW to the p-type substrate. The PN junction with the BPW and BNW1 makes a built-in-potential and it acts as a potential barrier that suppresses the punch-through between the BPW and the p-type substrate. The BNW1 also forms a lateral electric field to gather carriers generated in the sensor layer into the sense node [13]. The other buried n-well (BNW2) exists slightly under the BNW1. In the lateral direction, the BNW2 covers only the central portion of a pixel to further enhance the lateral electric field. It is introduced in XRPIX8 for the first time based on the result that the charge collection efficiency degraded near the pixel boundary in the previous prototype XRPIX with the PDD structure [17].

XRPIX8 has  $96 \times 96$  pixels, and the pixel size is  $36 \mu\text{m} \times 36 \mu\text{m}$ . Pixels at the outer edge of the pixel array are dummy pixels to suppress the interference from peripheral region. Therefore, pixels for X-ray detection are  $94 \times 94$  pixels, of which  $14 \times 94$  pixels are test element groups (TEG) having different circuit configurations.

### 3. Simulation study and fabrication of candidate chips

#### 3.1. Simulation study of n-well dopant concentration

The potential barrier height depends on the n-well dopant concentration and  $V_{\text{bb}}$ . We made a simulation study on the potential barrier behavior with different dopant concentrations of BNW1 using the TCAD tools (HyENEXSS<sup>1</sup>) [18, 19, 20, 21]. Referring to the operating condition of the previous prototype XRPIX with the PDD structure, in this simulation,  $V_{\text{bb}}$  and  $V_{\text{BPW}}$  were set to  $-300 \text{ V}$  and  $-2.5 \text{ V}$ , respectively.

Figure 2(a) shows potential profiles along A–A' in Figure 1, a vertical line from BPW to substrate crossing BNW1. We performed simulations by increasing dopant concentrations of BNW1 from the “reference” value. Here, the reference value indicates the dopant concentration of BNW1 of the previous prototype XRPIX with the PDD structure [14]. The dopant concentration of BNW2 was constant at the reference value through the simulations. The potential barrier height of BNW1 increases as the dopant concentration increases. Figure 2(b) shows a simulated current density map under the reference condition of BNW1. A large leakage current from the BPW to the substrate appeared because of punch-through. No leakage current appeared in the other conditions. These results suggest that the potential barrier height with the reference dopant concentration is insufficient to suppress punch-through. On the other hand, as stated above, the dopant concentration of BNW1 cannot be simply increased without consideration. The increase in dopant concentration would enlarge the neutralized BNW1 region, leading to short circuit between neighboring sense nodes via BNW1. The increase in dopant concentration would also narrow down the depletion region between the BNW1 and BPW, leading to an increase in sense-node capacitance.

We also performed simulations for the cases with or without BNW2. Figure 3 shows potential profiles along B–B' in Figure 1, a horizontal line crossing BNW2. The

potential shape near the pixel boundary is wider in the case with BNW2 compared to that without BNW2. This indicates that BNW2 would help to increase the charge collection efficiency near the pixel boundary. On the other hand, the introduction of BNW2 results in an increase in sense-node capacitance. It is also a subject of an optimization study between charge collection efficiency and spectroscopic performance.

#### 3.2. Fabrication of candidate chips

In order to experimentally perform an optimization study on the n-well dopant concentration, we fabricated five candidate chips based on the TCAD simulation results. All the chips were fabricated by using a  $0.2 \mu\text{m}$  fully-depleted SOI CMOS pixel process prepared by Lapis Semiconductor Co. Ltd. Table 1 shows the specification of the chips. XRPIX8.1 has the same dopant concentration of BNW1 as that of the reference value in TCAD simulation. Punch-through between the BPW and the substrate was expected to occur in XRPIX8.1 as predicted by the simulation result. From XRPIX8.2 to XRPIX8.4, the dopant concentration of BNW1 is increased in order by a factor of 0.5 with respect to that of XRPIX8.1. The dopant concentration of XRPIX8.2 was expected to be the lower limit that can prevent punch-through set by the TCAD simulation. Although XRPIX8.4 has sufficient dopant concentration to prevent punch-through, short circuit between the sense nodes via BNW1 might occur. The dopant concentration of BNW2 is the same as the reference value of BNW1. XRPIX8.5 has the same dopant concentration as that of XRPIX8.3 but does not have BNW2 for performance comparison. Only XRPIX8.5 does not have BNW2 as shown in Table 1.

## 4. Experiments and results

#### 4.1. Basic characteristics

Figure 4 shows  $I$ - $V_{\text{bb}}$  characteristics of the five candidate chips at room temperature. The  $I$ - $V_{\text{bb}}$  characteristic of XRPIX8.1 deviates from others with  $V_{\text{bb}}$  greater than  $-50 \text{ V}$ . This indicates that punch-through between the BPW and the substrate occurred due to a low potential barrier of XRPIX8.1 as suggested by our TCAD simulation. Other chips have breakdown voltages greater than  $-300 \text{ V}$ , which is large enough for full depletion. Results for leakage current suppression are summarized in Table 2.

Figure 5 shows raw-value maps and histograms in a single frame obtained with XRPIX8.1 and XRPIX8.4 with  $V_{\text{bb}}$  of  $-5 \text{ V}$  at room temperature. Here, the raw

<sup>1</sup>HyENEXSS is managed by TCAD Academic Council. E-mail address: tac@appi.keio.ac.jp

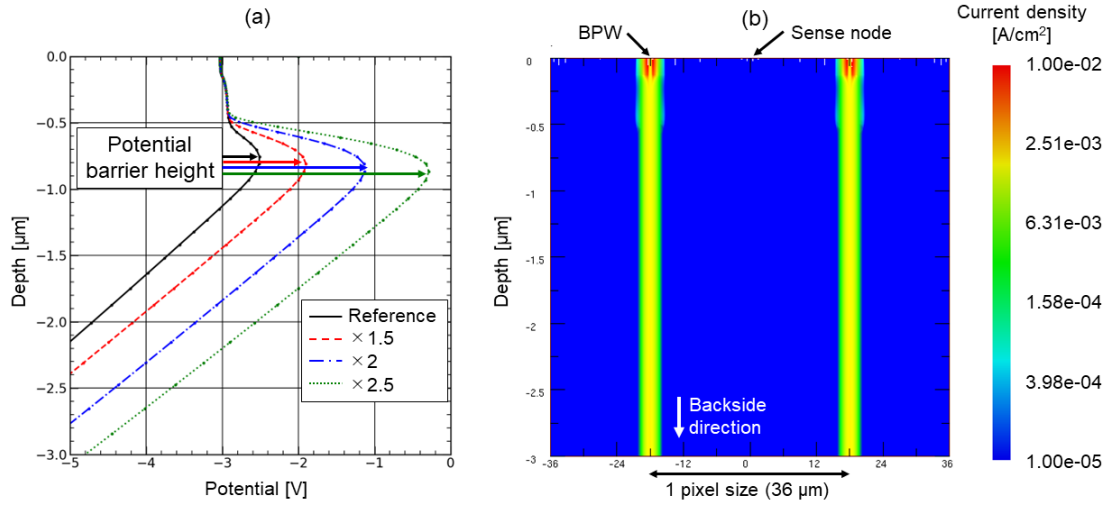


Figure 2: (a) Simulated potential profiles along line A-A' in Figure 1 with several different dopant concentrations of BNW1. That with the reference value of the dopant concentration of BNW1 is shown in black solid line. Those with 1.5, 2.0, and 2.5 times the reference value are shown in red dashed, blue dash-dot and green dotted lines, respectively. The arrows correspond to the potential barrier height of BNW1. (b) Simulated current density map under the reference condition of BNW1.

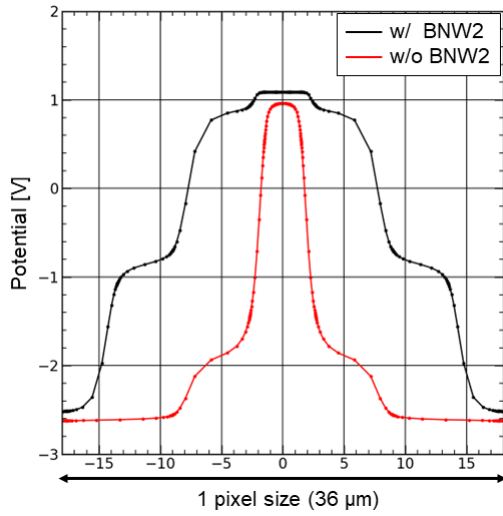


Figure 3: Simulated potential profile along line B-B' in Figure 1 with BNW2 (black) and without BNW2 (red)

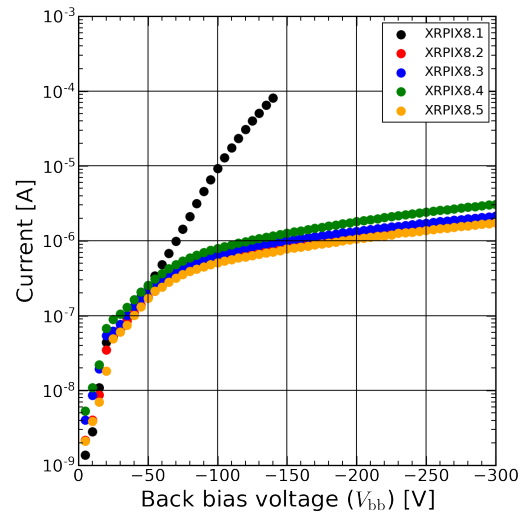


Figure 4:  $I$ - $V_{bb}$  characteristics of the five candidate chips at room temperature.

Table 1: Specification of candidate chips

Chip ID	BNW1: Dopant concentration	BNW2: Presence
XRPIX8.1	Reference ( $\times 1$ )	Yes
XRPIX8.2	$\times 1.5$	Yes
XRPIX8.3	$\times 2.0$	Yes
XRPIX8.4	$\times 2.5$	Yes
XRPIX8.5	$\times 2.0$	No

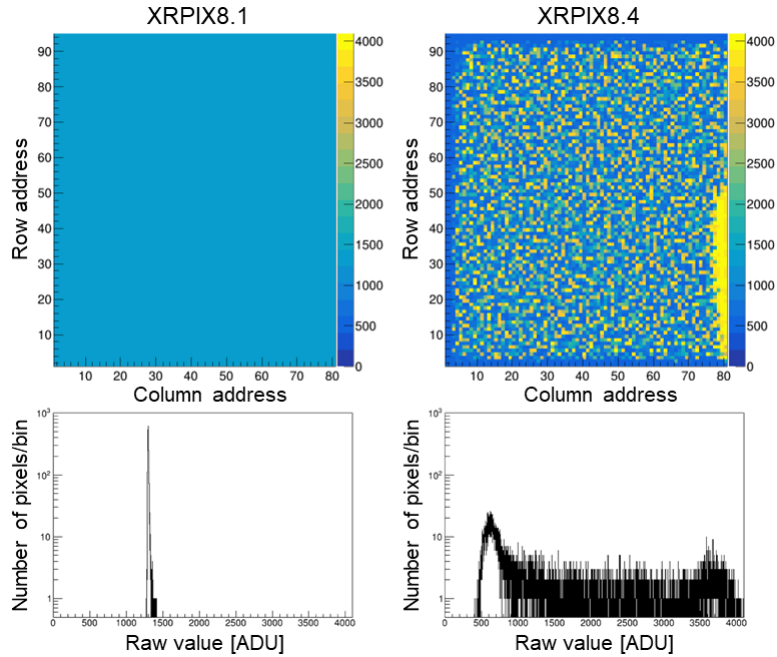


Figure 5: Raw-value maps and histograms in a single frame obtained with XRPIX8.1 (left) and XRPIX8.4 (right) with  $V_{bb}$  of  $-5$  V at room temperature. These figures do not include the dummy pixels and the TEG-region pixels. The high raw-value region in the bottom right of the map of XRPIX8.4 is likely affected by the TEG-region pixels at column addresses greater than 80 in which circuit configurations are further different above and below row address of 48.

value corresponds to the analog output of each pixel. The chips were not irradiated with X-rays. The raw value of XRPIX8.4 significantly spatially varies compared to that of XRPIX8.1. Other chips had spatial variations similar to XRPIX8.1. The large spatial variation of raw value in XRPIX8.4 was improved by applying larger  $V_{bb}$ , which promotes the depletion of BNW1 under the BPW. This result suggests that short circuit between the sense nodes via BNW1 occurs in the case of the high dopant concentration of BNW1 at low  $V_{bb}$ . It is not preferable that use of chip is limited with large  $V_{bb}$ . The dopant concentration of BNW1 is therefore desired to be less than 2.5 times the reference value to prevent short circuit between the sense nodes via BNW1.

#### 4.2. Spectroscopic Performance

Figure 6 shows  $^{57}\text{Co}$  spectra obtained with the five candidate chips at  $-60$  °C. In this experiment, the chips were irradiated from the front side with X-rays/ $\gamma$ -rays from  $^{57}\text{Co}$ . Each spectrum was taken from one specific pixel that showed the best performance among the pixels measured. In the data analysis, a pedestal value in a given frame was calculated as a running average of 50 raw values before and after the frame. A pedestal-

subtracted-raw value was recorded as a pulse height. Therefore, when no X-rays are detected, the pulse height histogram of the “X-ray-non-detected pixels” is a Gaussian-like distribution centered around zero, and the width of the distribution can be a measure of read-out noise. We used the standard deviation of the Gaussian function fitted to the distribution to determine two thresholds. One threshold is the event threshold for X-ray detection and is set to 10 sigma. It corresponds to the lower energy threshold of the chips. The other is the split threshold for charge-sharing events and set to 3 sigma. We used only single-pixel events, where signal charges are collected within one pixel and no charge sharing with neighboring pixels occurs with the split threshold. We applied  $V_{bb}$  of  $-300$  V, which is large enough for full depletion, to all the chips except for XRPIX8.1. Due to the large leakage current caused by punch-through between the BPW and the substrate,  $V_{bb}$  applied to XRPIX8.1 was limited to  $-200$  V, which is still close to the full depletion voltage. Three lines from  $^{57}\text{Co}$  (6.4, 7.1, and 14.4 keV) are seen in each spectrum. The relationship between the pulse height,  $PH$ , and the energy,  $E$ , of these lines are expressed as  $PH = aE + b$ . Each spectrum is shifted by  $b$  so that the line center

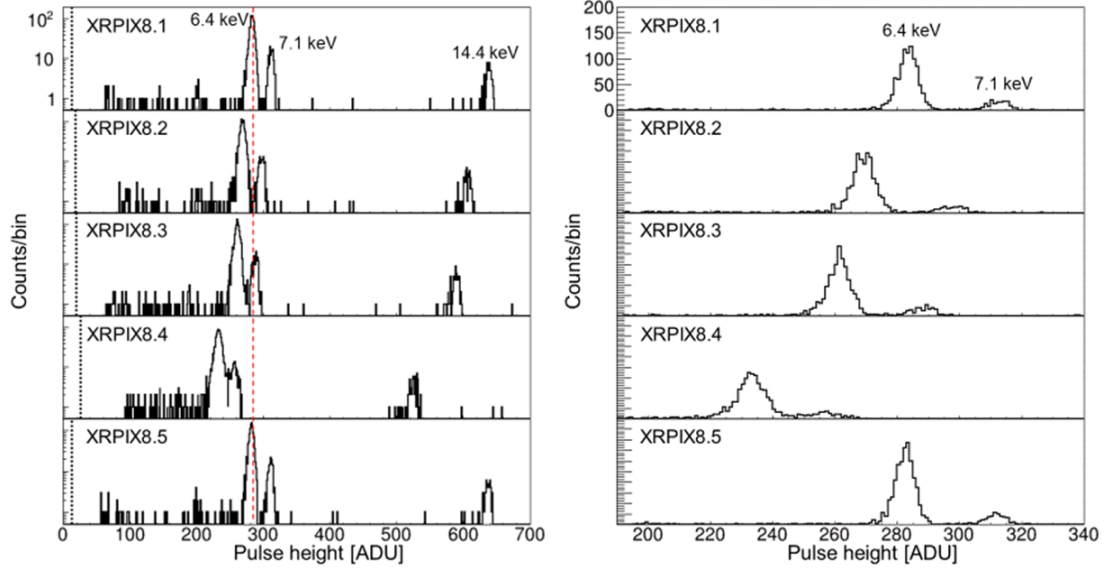


Figure 6:  $^{57}\text{Co}$  spectra obtained with the five candidate chips. The vertical axis in the left figure is a log scale to see the entire spectrum and the right figure is a linear scale to see a spectral line shape. Each spectrum was taken from one specific pixel and only single-pixel events were used. The black dotted line denotes the event threshold. The red dashed line denotes the line center of 6.4 keV in the spectrum of XRPIX8.1 for eye guide.

in the unit of ADU simply indicates  $a$ , namely overall gain. The amount of  $b$  measured did not correlate with the chip ID. From comparison among these spectra, it is clear that the line centers shift toward lower pulse height from XRPIX8.1 to XRPIX8.4 and get back to the level similar to XRPIX8.1 in XRPIX8.5. In addition, the line widths become larger from XRPIX8.1 to XRPIX8.4 and again get back to the level similar to XRPIX8.1 in XRPIX8.5.

Table 2 summarizes the output gain ( $G_{\text{OUT}}$ ) and energy resolution at 6.4 keV.  $G_{\text{OUT}}$  is calculated from  $a$  in the equation shown above, using that 1 ADU corresponds to 448  $\mu\text{V}$  and that the mean ionization energy per electron-hole pair in silicon is 3.65 eV [22]. The energy resolution represents FWHM of the 6.4 keV line. XRPIX8.1 and XRPIX8.5 show a satisfactory X-ray spectroscopic performance considering results obtained with previous XPIX chips [14]. These numbers are actually good enough as a general silicon detector although not the best. On the other hand, as can be seen from the spectra in Figure 6, these performance gradually degrades from XRPIX8.1 to XRPIX8.4.

Increase in dark current and/or readout noise can result in the degradation of the energy resolution. Dark current of each chip was measured following Kodama et al. [23]. The results measured at  $-60^\circ\text{C}$  are also summarized in Table 2. It is indicated that the dark current

does not correlate with chip ID unlike the energy resolution and is not a major source of the degradation of the energy resolution. Figure 7 shows the pulse height distributions of X-ray-non-detected pixels of the chips. The histogram width in Figure 7 becomes larger from XRPIX8.1 to XRPIX8.4 and get back to the level similar to XRPIX8.1 in XRPIX8.5. These results suggest that the increase in readout noise mainly degrades the energy resolution.

All the five candidate chips except for XRPIX8.5 have BNW2, which is introduced for an improvement of charge collection efficiency. Insufficient charge collection efficiency typically results in a low-energy tail of spectral lines, which make a spectral line asymmetric [17]. A comparison among the spectra in Figure 6 indicates that the symmetry degrees of the lines do not change with or without BNW2. This result suggests that the introduction of BNW2 is not of critical importance in terms of charge collection efficiency.

Table 2 digests the experimental results presented here. We found that the n-well design of XRPIX8.5 can make a potential barrier high enough to suppress a leakage current and also provide satisfactory X-ray spectroscopic performance. The detailed evaluation on the spectroscopic performance of XRPIX8.5 is presented elsewhere.

Table 2: Performance summary of the five candidate chips

Chip ID	Suppression of leakage current	Output gain [ $\mu\text{V}/e^-$ ]	Energy resolution at 6.4 keV (FWHM) [eV]	Dark current [ADU/ms]
XRPIX8.1	No	$39.42 \pm 0.06$	$166 \pm 5$	$(2.46 \pm 0.09) \times 10^{-1}$
XRPIX8.2	Yes	$37.56 \pm 0.07$	$202 \pm 5$	$(1.82 \pm 0.21) \times 10^{-1}$
XRPIX8.3	Yes	$36.43 \pm 0.07$	$208 \pm 6$	$(2.76 \pm 0.40) \times 10^{-1}$
XRPIX8.4	Yes	$32.57 \pm 0.08$	$296 \pm 9$	$(2.92 \pm 0.55) \times 10^{-1}$
XRPIX8.5	Yes	$39.38 \pm 0.05$	$166 \pm 4$	$(4.35 \pm 0.11) \times 10^{-1}$

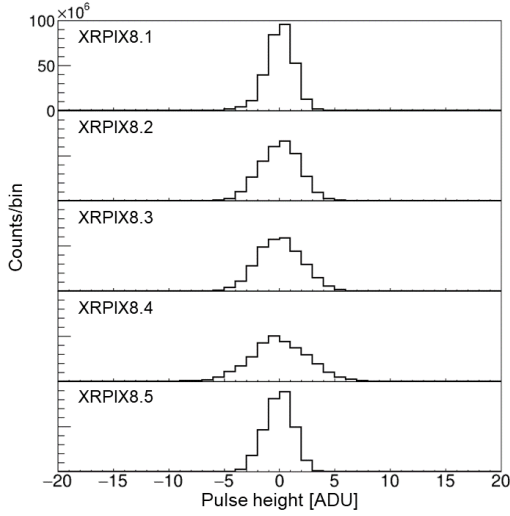


Figure 7: Pulse height distributions of X-ray-non-detected pixels of the five candidate chips.

## 5. Discussion

From the experimental results in section 4.2, we found that  $G_{\text{OUT}}$  and the energy resolution gradually degrade from XRPIX8.1 to XRPIX8.4 and get back to the level similar to XRPIX8.1 in XRPIX8.5. In this section, we discuss this tendency in more detail.

XRPIX has a charge-sensitive amplifier (CSA) and a source follower (SF) in a pixel circuit [24]. Therefore,  $G_{\text{OUT}}$  is a product of the CSA gain ( $G_{\text{CSA}}$ ), the SF gain ( $G_{\text{SF}}$ ), and the readout gain ( $G_{\text{RO}}$ ) that is a resultant gain of the readout circuit of chip and instrumentation amplifier on our evaluation board, which is written as

$$G_{\text{OUT}} = G_{\text{CSA}} \times G_{\text{SF}} \times G_{\text{RO}}. \quad (1)$$

Here,  $G_{\text{SF}}$  was 0.95 from the circuit simulation and  $G_{\text{RO}}$  was 0.70 from an experimental measurement.  $G_{\text{CSA}}$  is defined as a ratio of output voltage to input charge in the

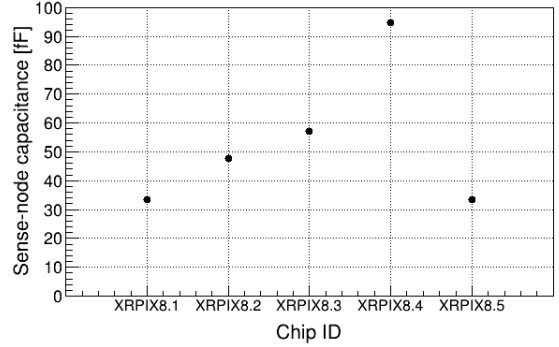


Figure 8: Sense-node capacitance ( $C_{\text{D}}$ ) calculated of the five candidate chips.

unit of elementary charge and is written as

$$G_{\text{CSA}} = q \frac{A_{\text{CS}}}{C_{\text{D}} + C_{\text{i}} + (A_{\text{CS}} + 1)C_{\text{FB}}}. \quad (2)$$

Here,  $q$  is the elementary charge in coulomb,  $C_{\text{D}}$  is the sense-node capacitance,  $A_{\text{CS}}$ ,  $C_{\text{i}}$  and  $C_{\text{FB}}$  are open-loop gain, input capacitance, and feedback capacitance in the CSA, respectively.  $A_{\text{CS}}$  was designed to 108 [25].  $C_{\text{i}}$  and  $C_{\text{FB}}$  were estimated to be 7.85 fF and 2.3 fF, respectively, by using the parasitic capacitance extractor tool. Figure 8 shows  $C_{\text{D}}$  of the five candidate chips, calculated using the  $G_{\text{OUT}}$  in Table 2 and Equations (1) and (2).  $C_{\text{D}}$  monotonically increases from XRPIX8.1 to XRPIX8.4 and decreases to the level similar to XRPIX8.1 in XRPIX8.5. This trend is naturally interpreted as due to the variation in n-well dopant concentration around a sense node. From XRPIX8.1 to XRPIX8.4, the dopant concentration of BNW1 increases monotonically and that of BNW2 is constant, resulting in a monotonic increase of sense-node capacitance. XRPIX8.5 does not have BNW2 and its dopant concentration of BNW1 is the same as that of XRPIX8.3, resulting in the level of node capacitance similar to that of XRPIX8.1.

The relation between the energy resolution

( $\Delta E_{\text{FWHM}}$ ) and readout noise ( $\sigma_R$ ) is written as

$$\Delta E_{\text{FWHM}} = 2 \sqrt{2 \ln 2} W \sqrt{\frac{FE}{W} + \sigma_R^2}. \quad (3)$$

Here,  $E$ ,  $F$ , and  $W$  are the incident X-ray energy, the Fano factor of 0.128 [26], and the mean ionization energy per electron-hole pair in silicon of 3.65 eV, respectively. We first measured  $\Delta E_{\text{FWHM}}$  of the three lines in Figure 6 and derived  $\sigma_R$  by fitting the data of “ $\Delta E_{\text{FWHM}}$  vs  $E$ ” with equation (3).

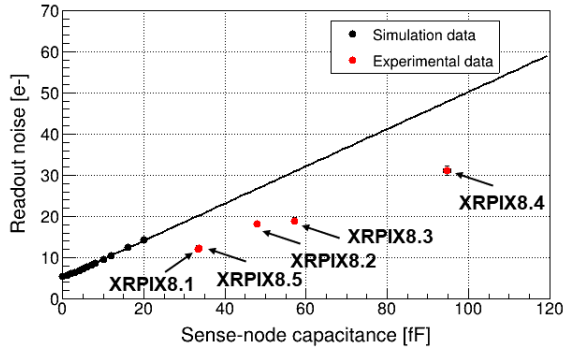


Figure 9: Readout noise ( $\sigma_R$ ) as a function of the sense-node capacitance ( $C_D$ ). The red points and black points are experimental and simulation data, respectively. The black solid line is the fitting model (linear function) of simulation data.

Figure 9 plots  $\sigma_R$  as a function of  $C_D$ . We also performed a circuit simulation to estimate  $\sigma_R$ , in which we found that the flicker noise of the input transistor in the CSA almost dominates the entire value. Figure 9 also shows  $\sigma_R$  as a function of  $C_D$  obtained by the circuit simulation. The  $C_D$  dependencies of  $\sigma_R$  obtained by our experiment and circuit simulation reasonably match, suggesting that the variation of the energy resolution can be also explained by that of the sense-node capacitance. On the other hand, there is a certain difference between the experiment and simulation values. We consider that it might be due to the inaccuracy of  $C_{\text{FB}}$ . The feedback capacitance in the CSA largely depends on the Metal-Oxide-Metal (MOM) capacitance between metal wires so that the MOM capacitance is subject to small-scale manufacturing variations in the layout and figure of the metal wires. Therefore,  $C_{\text{FB}}$  extracted from the designed layout may not accurately reflect the real value. From Equation (2), a small increase in  $C_{\text{FB}}$  leads to a large decrease in  $C_D$ , resulting in smaller differences between the experiment and simulation values. We plan to implement TEG to measure  $C_{\text{FB}}$  experimentally in the next chip.

## 6. Conclusion

An optimization study on the n-well dopant concentration in the XRPIX with a PDD structure was performed. Five candidate chips were fabricated based on the TCAD simulation, focusing on the potential barrier height between the pinned p-well and p-type substrate and also on the sense-node capacitance. The best n-well design was successfully found out in which a large leakage current was surely suppressed and satisfactory X-ray spectroscopic performance was obtained. The X-ray spectroscopic performance actually depends on the dopant concentration and configuration of the n-well, which can be basically understood by the variation in sense node capacitance.

## 7. Acknowledgments

We acknowledge the valuable advice and the manufactures of XRPIXs by the personnel of LAPIS Semiconductor Co., Ltd. This study was supported by the Japan Society for the Promotion of Science (JSPS) KAKENHI, Grant-in-Aid for Scientific Research on Innovative Areas 25109004 (T.G.T., T.T., K.M., A.T., and T.K.), Grant-in-Aid for Scientific Research (A) 15H02090 (T.G.T. and A.T.) and 21H04493 (T.G.T., T.T. and A.T.), Grant-in-Aid for Scientific Research (B) 21H01095 (K.M.), 22H01269 (T.K. and K.H.) and by JST SPRING, Grant Number JPMJSP2105. This study was also supported by the VLSI Design and Education Center (VDEC), the University of Tokyo in collaboration with Cadence Design Systems, Inc., and Mentor Graphics, Inc.

## References

- [1] B. E. Burke, et al., CCD soft x-ray imaging spectrometer for the ASCA satellite, *IEEE Transactions on Nuclear Science* 41 (1) (1994) 375–385.
- [2] G. P. Garmire, et al., Advanced CCD imaging spectrometer (ACIS) instrument on the Chandra x-ray observatory, in: *Proceedings of SPIE* 4851 (2003) 28–44.
- [3] M. J. L. Turner, et al., The european photon imaging camera on XMM-Newton: The MOS cameras, *Astronomy and Astrophysics* 365 (1) (2001) L27–L35.
- [4] K. Koyama, et al., X-ray imaging spectrometer (XIS) on board Suzaku, *Publications of the Astronomical Society of Japan* 59 (2007) S23–S33.
- [5] H. Tomida, et al., Solid-state slit camera (SSC) aboard MAXI, *Publications of the Astronomical Society of Japan* 63 (2011) 397–405.
- [6] T. Tanaka, et al., Soft x-ray imager aboard Hitomi (ASTRO-H), *Journal of Astronomical Telescopes, Instruments, and Systems* 4 (1) (2018).

- [7] K. Mori, et al., Xtend, the soft x-ray imaging telescope for the x-ray imaging and spectroscopy mission (XRISM), in: Proceedings of SPIE 12181 (2022).
- [8] M. Bautz, et al., Progress toward fast, low-noise, low-power CCDs for Lynx and other high-energy astrophysics missions, in: Proceedings of SPIE 11444 (2020).
- [9] T. G. Tsuru, H. Hayashi, K. Tachibana, et al., Kyoto's event-driven x-ray astronomy SOI pixel sensor for the FORCE mission, in: Proceedings of SPIE 10709 (2018).
- [10] Y. Arai, T. Miyoshi, Y. Unno, et al., Development of SOI pixel process technology, Nuclear Instruments and Methods in Physics Research Section A: Accelerators, Spectrometers, Detectors and Associated Equipment 636 (2011) S31–S36.
- [11] A. Takeda, Y. Arai, S. G. Ryu, et al., Design and evaluation of an SOI pixel sensor for trigger-driven x-ray readout, IEEE Transactions on Nuclear Science 60 (2) (2013) 586–591.
- [12] T. G. Tsuru, H. Matsumura, A. Takeda, et al., Development and performance of kyoto's x-ray astronomical SOI pixel (SOIPIX) sensor, in: Proceedings of SPIE 9144 (2014) 914412.
- [13] H. Kamehama, S. Kawahito, S. Shrestha, et al., A low-noise x-ray astronomical silicon-on-insulator pixel detector using a pinned depleted diode structure, Sensors 18 (1) (2018) 27.
- [14] S. Harada, T. G. Tsuru, T. Tanaka, et al., Performance of the silicon-on-insulator pixel sensor for x-ray astronomy, XRPIX6E, equipped with pinned depleted diode structure, Nuclear Instruments and Methods in Physics Research Section A: Accelerators, Spectrometers, Detectors and Associated Equipment 924 (2019) 468–472.
- [15] M. Hayashida, K. Hagino, T. Kohmura, et al., Proton radiation hardness of x-ray SOI pixel sensors with pinned depleted diode structure, Journal of Astronomical Telescopes, Instruments, and Systems 7 (3) (2021).
- [16] K. Hagino, M. Kitajima, T. Kohmura, et al., Radiation-induced degradation mechanism of x-ray SOI pixel sensors with pinned depleted diode structure, IEEE Transactions on Nuclear Science 70 (7) (2023) 1444–1450.
- [17] K. Kayama, T. G. Tsuru, T. Tanaka, et al., Subpixel response of SOI pixel sensor for x-ray astronomy with pinned depleted diode: first result from mesh experiment, Journal of Instrumentation 14 (2019) C06005.
- [18] Keio University TCAD Research and Development Center, 3D TCAD Simulator HyENEXSS ver. 8.5K (2019).
- [19] N. Kotani, TCAD in Selete, in: Proc. Int. Conf. Simulation of Semiconductor Processes and Devices, SISPAD'98, Leuven, Belgium, 1998, pp. 3–7.
- [20] T. Wada, et al., Enexss a 3-dimensional tcad system, in: Ext. Abstr. 53rd Spring Meeting, Japan Society of Applied Physics, 2006, pp. 22p–ZA–2, [in Japanese].
- [21] M. Nakamura, Current status and subjects on practical 3d TCAD for next generation, Monthly Publication of The Japan Society of Applied Physics 77 (7) (2008) 818, [in Japanese].
- [22] J. R. Janesick, Scientific Charge-Coupled Devices, SPIE, 2001.
- [23] R. Kodama, T. G. Tsuru, T. Tanaka, et al., Low-energy x-ray performance of SOI pixel sensors for astronomy, "XRPIX", Nuclear Instruments and Methods in Physics Research Section A: Accelerators, Spectrometers, Detectors and Associated Equipment 986 (2021) 164745.
- [24] A. Takeda, T. G. Tsuru, T. Tanaka, et al., Improvement of spectroscopic performance using a charge-sensitive amplifier circuit for an x-ray astronomical SOI pixel detector, Journal of Instrumentation 10 (06) (2015) C06005.
- [25] A. Takeda, K. Mori, Y. Nishioka, et al., Spectroscopic performance improvement of SOI pixel detector for x-ray astronomy by introducing double-SOI structure, Journal of Instrumentation 15 (11) (2020) 11001.
- [26] I. V. Kotov, et al., Pair creation energy and fano factor of silicon measured at 185 k using x-rays, Nuclear Instruments and Methods in Physics Research Section A: Accelerators, Spectrometers, Detectors and Associated Equipment 901 (2018) 126–132.